INORGANIC CHEMISTRY FRONTIERS

RESEARCH ARTICLE

View Article Online
View Journal | View Issue

Cite this: *Inorg. Chem. Front.*, 2026, **13**, 1931

Gd/Tb/Eu alloyed double-perovskite lanthanide halides for color tunable photoluminescence and robust scintillation performance

Su Zhou, * Linshuai Li, Gaoqing Chen, Jingtao Zhao and Lei Lei

Double-perovskite materials with diverse elemental compositions have been developed as high-performance phosphors and scintillators. However, the low doping concentration of activator ions in the host matrix limits the flexible tuning of luminescence properties. In this work, we propose a series of gadolinium, terbium, and europium alloyed double-perovskite lanthanide chlorides (DPLCs) to achieve color-tunable photoluminescence (PL) as well as thermally and radiationally stable X-ray excited optical luminescence (XEOL). The $Cs_2NaGdCl_6$ host allows up to 100% and 60% doping concentrations of Tb^{3+} ions for PL and XEOL, respectively, without concentration quenching. The designed $Cs_2NaTbCl_6$ exhibits a high photoluminescence quantum yield of 73.5%. Optical encryption was achieved using $Cs_2NaTb_{0.95}Eu_{0.05}Cl_6$, which shows excitation-wavelength-dependent dynamic emission colors. Benefiting from efficient energy transfer from Gd^{3+} to Tb^{3+} in the XEOL process, $Cs_2NaGd_{0.4}Tb_{0.6}Cl_6$ achieves a high light yield of 27 000 ph MeV^{-1}. With the incorporation of Eu^{3+}, $Cs_2NaTbGd_{0.35}Tb_{0.6}Eu_{0.05}Cl_6$ exhibits excellent thermal and radiation stability for scintillation. Moreover, DPLCs embedded in polymethyl methacrylate (PMMA) scintillator films enable high-resolution X-ray imaging with a spatial resolution of 16.6 lp mm^{-1}. This work provides a novel strategy for designing DPLCs with state-of-the-art optical applications.

Received 28th October 2025,
Accepted 16th December 2025

DOI: 10.1039/d5qi02185e

rsc.li/frontiers-inorganic

Introduction

Double-perovskite metal halides (DPMHs), known for their low-toxicity chemical components and stable crystal structures, have attracted extensive research interest due to their extraordinary luminescence properties, particularly in applications such as advanced light-emitting diodes, scintillators, and optical sensing.[1–8] As derivatives of the perovskite structure, DPMHs are formed by replacing two Pb^{2+} ions with one monovalent cation (M^+) and one trivalent cation (M^{3+}), resulting in $[M^+X_6]$ and $[M^{3+}X_6]$ octahedral units that collectively constitute a three-dimensional double perovskite structure with the general formula $A_2M^+M^{3+}X_6$. Theoretically, this framework offers considerable compositional flexibility: M^+ can be Ag^+, Na^+, or Cu^+, while M^{3+} may include Bi^{3+}, Sb^{3+}, or In^{3+}. This enables the design of diverse perovskite materials such as Cs_2AgBiX_6, $Cs_2AgInCl_6$, $Cs_2AgSbCl_6$, and $Cs_2NaBiCl_6$, as well as their alloyed variants.[9–13] Despite their promise, these materials face significant challenges in spectral modulation due to intrinsic self-trapped emissions in DPMHs. To address these limitations, novel strategies such as ion doping have been successfully employed to broaden the spectral range and enhance emission intensity. For example, Mn^{2+} doping can induce broad white emission with a high photoluminescence quantum yield (PLQY), while lanthanide ions like Er^{3+}, Nd^{3+}, and Yb^{3+} enable near-infrared emission in DPMHs.[14–18] Although these advances have expanded both the spectral range and quantum efficiency of DPMHs, the achievement of narrow-band pure-color emission in DPMH hosts remains an area requiring further development.

In recent years, double-perovskite lanthanide chlorides (DPLCs) with the formula $Cs_2NaLnCl_6$ have been proposed for high-performance optical applications.[19,20] Through diverse activator doping in the DPLC host, multi-mode stimulated luminescence—including down-shifting, up-conversion, and X-ray emission—has been achieved.[21–25] Lanthanide ions possess distinctive 4f–4f and $4f^{n-1}$–5d inner-shell transitions, endowing them with exceptional photoelectric properties such as rich emission spectra, extremely narrow emission bandwidths, long luminescence lifetimes, and large Stokes shifts. Typically, increasing the doping concentration of luminescent centers leads to reduced radiative transition efficiency due to cross-relaxation between ions. However, owing to their unique crystal structure and large interatomic distances, DPLCs generally allow higher doping concentrations compared to lanthanide fluorides and oxides.[26–32] Notably, some DPLCs can

College of Optical and Electronic Technology, China Jiliang University, Hangzhou 310018, China. E-mail: zhousu@cjlu.edu.cn

accommodate lanthanide activators at nearly full concentrations. For example, Nie *et al.* reported that $C_2NaTb_{0.95}Sc_{0.05}Cl_6$ exhibits a high PLQY of 96.07% and stable luminescence under conditions of extreme temperature, humidity, and long-term UV exposure.[33] Sb^{3+}/Sm^{3+}-co-doped $Cs_2NaLuCl_6$ DPLCs achieve PLQYs of 74.58% in the visible region and 23.12% in the NIR region under optimal doping concentrations of 0.5%Sb^{3+} and 25%Sm^{3+}.[34] $Cs_2NaHoCl_6$ DPLCs show a high NIR PLQY of 82.3%, achieved by suppressing non-radiative recombination losses, resulting in robust photostability against thermal quenching.[35] Qiu and co-workers showed that $Cs_2Ag_{0.1}Na_{0.9}ErCl_6$ microcrystals exhibit NIR emission at 1540 nm with a PLQY of 90 ± 6% under 379 nm excitation and a large Stokes shift exceeding 1000 nm, while $Cs_2NaYb_{0.4}Er_{0.6}Cl_6$ microcrystals achieve a near-unity PLQY of 98.6% under 980 nm excitation.[36]

Furthermore, due to the high atomic numbers of Cs and lanthanide elements, DPLCs exhibit effective X-ray absorption and outstanding scintillator properties. The Tang group reported $Cs_2NaTbCl_6$ and $Cs_2NaEuCl_6$ single crystals with green and red emission, respectively, showing high light yields (LY) of 46 600 ph MeV^{-1} and 1250 ph MeV^{-1}.[37] With 60% Tb^{3+} doping, $Cs_2NaSc_{0.4}Tb_{0.6}Cl_6$ single crystals exhibited a near-unity PLQY of 98.2% and an intense afterglow lasting up to 12 hours after X-ray excitation ceases.[38] However, the critical doping concentration for luminescence quenching of Tb^{3+} in $Cs_2NaGdCl_6$ was notably low—only 5% for photoluminescence (PL) and 7% for radioluminescence (RL).[39] It is also worth noting that the luminescence performance of nano-sized DPLCs still lags behind their single-crystal counterparts; for instance, $Cs_2NaTbCl_6$ nanocrystals showed a PLQY of only 12% and a lower light yield.[40,41]

In this work, a series of gadolinium and terbium alloyed DPLCs, $Cs_2NaGd_{1-x}Tb_xCl_6$, at a sub-micron scale were prepared *via* a supersaturation recrystallization method at room temperature. These compounds exhibit a high quenching concentration of Tb^{3+} up to 100% for PL, along with a high PLQY of 73.5%. Based on the high-performance $Cs_2NaTbCl_6$, Eu^{3+} ions were introduced to tune the emission color. As the excitation wavelength shifts from 275 nm to 375 nm, the emission color of $Cs_2NaTb_{0.95}Eu_{0.05}Cl_6$ changes from orange to red to yellow. This excitation-dependent emission behavior enables applications in optical anti-counterfeiting using binary coding. Furthermore, $Cs_2NaGd_{1-x}Tb_xCl_6$ crystals exhibit outstanding scintillator performance. The quenching concentration of Tb^{3+} reaches 60% in $Cs_2NaGd_{0.4}Tb_{0.6}Cl_6$, yielding a high LY of 27 000 ph MeV^{-1}. With the introduction of Eu^{3+}, $Cs_2NaGd_{0.35}Tb_{0.6}Eu_{0.05}Cl_6$ crystals exhibit robust RL under long-term radiation exposure. Interestingly, thermal enhancement of RL and ratiometric luminescence between Eu^{3+} and Tb^{3+} with increasing temperature were observed. Using the high-performance scintillator $Cs_2NaGd_{0.35}Tb_{0.6}Eu_{0.05}Cl_6$, a polymethyl methacrylate (PMMA) film was fabricated, achieving X-ray imaging with a high resolution of 16.6 lp mm^{-1}. This work provides a novel strategy for developing high-performance DPLC luminescent materials for advanced optical applications.

Results and discussion

A series of DPLC crystals were synthesized *via* a supersaturation recrystallization (SR) method, using an environmentally friendly solution system with deionized (DI) water as the solvent and a mixture of ethanol and ethyl acetate as the anti-solvent (see details in the Experimental section, SI). As illustrated in the schematic diagram in Fig. 1a, the cubic-phase $Cs_2NaTbCl_6$ crystallizes in the $Fm\bar{3}m$ space group, wherein the hexacoordinated octahedral [$TbCl_6$] units provide an optimal coordination environment for luminescence from trivalent lanthanide ions.[42,43] The SR-synthesized products consist of a pure phase of $Cs_2NaTbCl_6$, as confirmed by the XRD pattern matching the standard ICDD card (#00-055-0604) with no detectable impurities or secondary phases (Fig. 1b). Under 275 nm UV light or X-ray irradiation, the samples exhibit strong green emission (Fig. 1c). Scanning electron microscopy (SEM) images (Fig. 1d and e) show that the $Cs_2NaTbCl_6$ powder possesses a polyhedral morphology, with grain sizes predominantly within 1 μm (Fig. S1, SI). EDS elemental mapping of single particle $Cs_2NaTbCl_6$ with a homogeneous distribution of its constituent elements is shown in Fig. S2 (SI).

X-ray photoelectron spectroscopy (XPS) was employed to further analyze the chemical composition of $Cs_2NaTbCl_6$. The survey spectrum (Fig. 1f) shows characteristic binding energy peaks corresponding to Tb 3d, Na 1s, Cs 3d, and Cl 2p, confirming the presence of Tb^{3+}, Na^+, Cs^+, and Cl^-. High-resolution XPS spectra of elements are shown in Fig. S3. Specifically, the Tb $3d_{3/2}$ peaks were fit at 1277.2 eV, while the $3d_{5/2}$ peaks were observed at 1243.6 eV and 1240.8 eV, consistent with reported values. The Cl 2p spectrum shows characteristic doublet peaks at 200.0 eV ($2p_{1/2}$) and 198.5 eV ($2p_{3/2}$). For the monovalent cations, the Cs 3d peaks were located at 738.4 eV ($3d_{3/2}$) and 724.5 eV ($3d_{5/2}$), and the Na 1s peak was observed at 1071.9 eV.

The PL and photoluminescence excitation (PLE) spectra are shown in Fig. S4 (SI). The PLE spectrum exhibits a broad band

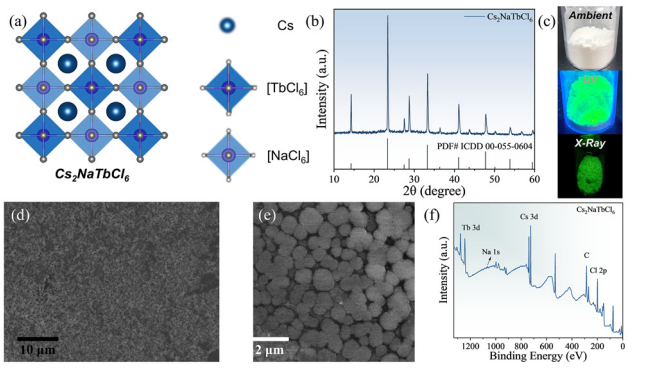

Fig. 1 (a) Schematic illustration of $Cs_2NaTbCl_6$ crystals with a double-perovskite structure. (b) The XRD pattern of the prepared $Cs_2NaTbCl_6$ matches the standard card. (c) Images of $Cs_2NaTbCl_6$ under ambient light, UV and X-ray. (d) and (e) SEM image of the $Cs_2NaTbCl_6$ crystals and their high magnification images. (f) XPS survey results of $Cs_2NaTbCl_6$.

from 270 to 300 nm, which is attributed to the transition from the valence band (VB) to the conduction band (CB), where the VB consists primarily of Cl 3p orbitals and the CB is formed by Tb 5d orbitals.[22,25,27] Additionally, several weak narrow peaks between 300 and 400 nm are assigned to the f–f transitions of Tb^{3+}. In the PL spectrum, narrow emission peaks are observed at approximately 500 nm, 550 nm, 600 nm, and 625 nm, corresponding to the $^5D_4 \rightarrow {}^7F_6$, $^5D_4 \rightarrow {}^7F_5$, $^5D_4 \rightarrow {}^7F_4$, $^5D_4 \rightarrow {}^7F_3$ transitions of Tb^{3+} ions, respectively.

To further investigate the concentration quenching behavior in the DPLC host, a series of Gd–Tb alloyed compounds were synthesized by incorporating optically inert Gd^{3+} ions. XRD results confirm that no impurity phases were introduced as shown in Fig. S5 (SI). Due to the smaller ionic radius of Tb^{3+} (0.92 Å) compared to Gd^{3+} (0.94 Å), the diffraction peaks shift to higher angles with increasing Tb^{3+} concentration. The luminescence properties of $Cs_2NaGd_{1-x}Tb_xCl_6$ were systematically studied. Fig. 2a shows the PL spectra under 275 nm excitation. The intensity of the green emission from the $^5D_4 \rightarrow {}^7F_J$ transitions increases gradually with higher Tb^{3+} doping levels, whereas the blue emission from the $^5D_3 \rightarrow {}^7F_J$ transitions decreases correspondingly. As clearly shown in Fig. 2b, the $^5D_3$-related emission is progressively suppressed with increasing Tb^{3+} content. Quantitative analysis indicates that the contribution of $^5D_3$ emission decreases dramatically from 22.4% to 1.9%, while that of $^5D_4$ emission increases from 77.6% to 98.1%. This strong anti-correlation clearly indicates efficient cross-relaxation between Tb^{3+} ions. The PLQY reaches 73.5% for $Cs_2NaTbCl_6$, originating from the highly radiative $^5D_4$ level, while $Cs_2NaGd_{0.9}Tb_{0.1}Cl_6$ shows a PLQY of only 25.6% (Fig. S6, SI), showing the high concentration quenching threshold of Tb^{3+} in the DPLC host. The transient PL lifetime was further measured to investigate the energy transfer process in $Cs_2NaGd_{1-x}Tb_xCl_6$. As shown in Fig. 2c, the lifetime of the $^5D_3$ level decreases with increasing Tb^{3+} concentration, decreasing from 2.52 ms to 19.6 μs (see Table S1, SI). This reduction can be attributed to efficient cross-relaxation between Tb^{3+} ions ($^5D_3 + {}^7F_6 \rightarrow {}^5D_4 + {}^7F_0$), as illustrated in Fig. 2d. Specifically, the $^5D_3$ lifetime decreases from 7.16 ms in $Cs_2NaGd_{0.9}Tb_{0.1}Cl_6$ to 6.29 ms in $Cs_2NaGd_{0.6}Tb_{0.4}Cl_6$ (Fig. S7, SI). However, no further decrease is observed at higher Tb^{3+} concentrations, indicating the absence of concentration quenching.

To further tailor the luminescence properties, 5% Eu^{3+} ions were incorporated into $Cs_2NaTbCl_6$ to achieve tunable emission colors. The excitation spectra of $Cs_2NaTb_{0.95}Eu_{0.05}Cl_6$ are presented in Fig. 3a. The excitation band monitored at 548 nm (corresponding to Tb^{3+} emission) is consistent with that of pure $Cs_2NaTbCl_6$. For Eu^{3+}, the excitation spectrum monitored at 596 nm comprises a broad band between 250 and 350 nm, attributed to the Cl–Eu charge transfer band, along with several narrow peaks in the 350–450 nm range, associated with the 4f–4f transitions of Eu^{3+}. The emission spectrum under 315 nm excitation—where only Eu^{3+} ions are excited—is shown in Fig. 3b, highlighting the characteristic photoluminescence of Eu^{3+}. The sample exhibits orange-red emission, with a prominent peak at 596 nm originating from the $^5D_0 \rightarrow {}^7F_1$ transition, and additional typical Eu^{3+} emissions between 611 and 624 nm corresponding to the $^5D_0 \rightarrow {}^7F_2$ transition. Benefiting from the distinct excitation characteristics of Tb^{3+} and Eu^{3+}, $Cs_2NaTb_{0.95}Eu_{0.05}Cl_6$ shows tunable emission colors. As depicted in Fig. 3b, varying the excitation wavelength from 275 nm to 375 nm alters the intensity ratio between Tb^{3+} and Eu^{3+} emission (I_{Tb}/I_{Eu}), leading to shifts in the overall emission profile. As the excitation wavelength increases from 275 nm to 305 nm, the I_{Eu}/I_{Tb} ratio gradually increases, with Eu^{3+} emission dominating between 305 nm and 335 nm. Upon further red-shifting to 375 nm, the emission intensities of Tb^{3+} and Eu^{3+} become comparable, yielding a balanced emission. As a result, the emitted color transitions sequentially from orange to red and finally to yellow. The color changes were further annotated using the Commission internationale de l'éclairage (CIE) coordinates as shown in Fig. 3c, as the position shifted from (0.49, 0.46) to (0.58, 0.37) and then to (0.40, 0.44).

Utilizing the excitation wavelength-dependent luminescence of $Cs_2NaTb_{0.95}Eu_{0.05}Cl_6$, we developed an optical encryption system based on binary coding that synergistically

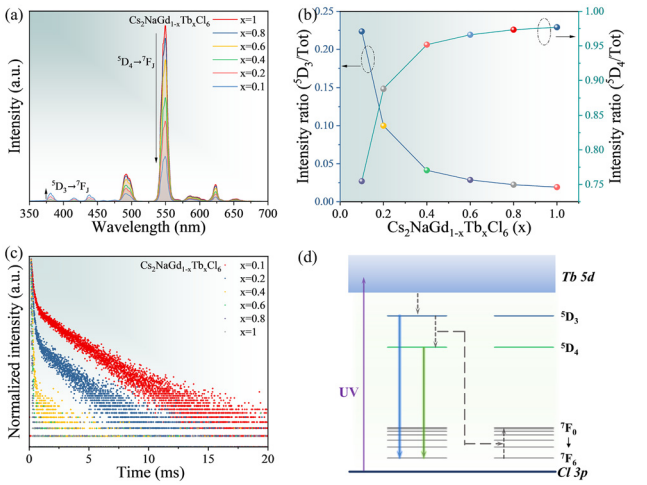

Fig. 2 (a) PL spectra of $Cs_2NaGd_{1-x}Tb_xCl_6$ under an excitation wavelength of 275 nm. (b) The emission ratio from $^5D_3$ and $^5D_4$ levels over total emission. (c) Photoluminescence decay curves for the $^5D_3$ level (437 nm). (d) Energy-level diagram for Tb^{3+} ions in $Cs_2NaGd_{1-x}Tb_xCl_6$ showing a possible route of luminescence quenching and cross-relaxation.

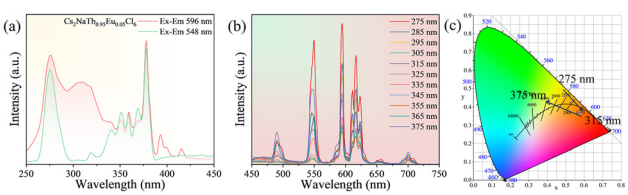

Fig. 3 (a) PLE spectra of Tb^{3+} ions (548 nm) and Eu^{3+} (596 nm). (b) PL spectra of $Cs_2NaTb_{0.95}Eu_{0.05}Cl_6$ under various excitation wavelengths. (c) CIE coordinates of the $Cs_2NaTb_{0.95}Eu_{0.05}Cl_6$ emission.

integrates $Cs_2NaTb_{0.95}Eu_{0.05}Cl_6$ and $Cs_2NaEuCl_6$. As evidenced in Fig. S8 (SI), under 315 nm UV irradiation, $Cs_2NaTb_{0.95}Eu_{0.05}Cl_6$ exhibits distinct orange emission, whereas $Cs_2NaEuCl_6$ maintains red luminescence; conversely, both compounds display homogeneous red emission at 365 nm excitation. Within this encryption system, we leveraged the dynamic PL color of DPLCs to implement binary state encoding. When subjected to modulated UV excitation wavelengths, a distinct emission color (from red to orange) was assigned to bit state "1", while unchanged emission profiles were designated as bit state "0". For demonstration in Fig. 4, capital letters "I K U N" are converted to binary sequences and spatially mapped onto a 4 × 8 matrix with $Cs_2NaTb_{0.95}Eu_{0.05}Cl_6$ and $Cs_2NaEuCl_6$ representing bit "1" and "0" positions, respectively (Fig. 4a). Under 365 nm UV (encryption mode), a uniform red emission conceals the information; during 315 nm decryption, elements exhibiting orange transition are decoded as "1", while persistently red-emitting elements register as "0", successfully reconstructing the original characters from the binary sequences 01001001 (I), 01001011 (K), 01010101 (U), and 01001110 (N) (Fig. 4b).

The scintillation properties of a series of $Cs_2NaGd_{1-x}Tb_xCl_6$ compounds were systematically investigated. The X-ray XEOL spectra are presented in Fig. 5a. In the Gd–Tb alloyed samples, a narrow emission peak with a full width at half maximum (FWHM) of 2.4 nm is observed at 312 nm in the UV region and is shown in Fig. S9, originating from the Gd^{3+} transition $^6P_{7/2} \rightarrow {}^8S_{7/2}$. Additional narrow peaks in the ranges of 350–450 nm and 475–650 nm are assigned to the $^5D_3 \rightarrow {}^7F_J$ and $^5D_4 \rightarrow {}^7F_J$ transitions of Tb^{3+} ions, respectively. The intensity ratio between the $^5D_4 \rightarrow {}^7F_J$ and $^5D_3 \rightarrow {}^7F_J$ emissions increases with Tb^{3+} concentration, consistent with their photoluminescence (PL) characteristics. A weak broad band between 350 and 450 nm in low Tb^{3+} concentration samples ($Cs_2NaGd_{0.9}Tb_{0.1}Cl_6$ and $Cs_2NaGd_{0.8}Tb_{0.2}Cl_6$) can be attributed to the self-trapped exciton (STE) emission of the host lattice. Taking the commercial scintillator $Bi_4Ge_3O_{12}$ (BGO) as a reference, a high LY of 27 000 photons ph MeV^{-1} was achieved in the $Cs_2NaGd_{0.4}Tb_{0.6}Cl_6$ sample, Fig. S10 (SI). We propose that Gd^{3+} introduces an intermediate energy level between the conduction band and the 4f levels of Tb^{3+}, thereby reducing energy loss during the transfer process.

Furthermore, Eu^{3+} ions were incorporated to achieve radiation-stable and temperature-dependent XEOL. The Eu^{3+} emission in the XEOL spectra (Fig. 5b), observed between 611 and

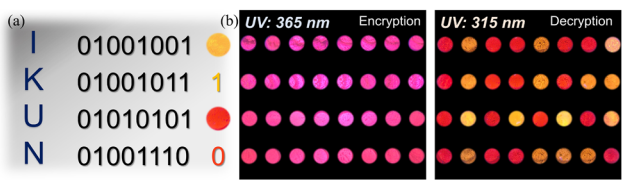

Fig. 4 (a) Binary sequences of the capital letters "I K U N". (b) Luminescence images of a 4 × 8 matrix with $Cs_2NaTb_{0.95}Eu_{0.05}Cl_6$ and $Cs_2NaEuCl_6$ under 365 nm and 315 nm.

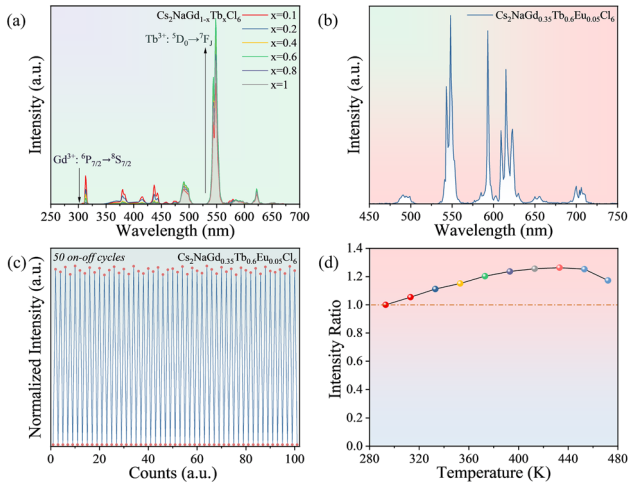

Fig. 5 The XEOL spectra of $Cs_2NaGd_{1-x}Tb_xCl_6$ (a) and $Cs_2NaGd_{0.35}Tb_{0.6}Eu_{0.05}Cl_6$ (b). (c) The XEOL intensity of $Cs_2NaGd_{0.35}Tb_{0.6}Eu_{0.05}Cl_6$ under long-term X-ray radiation showing stability. (d) The integrated XEOL intensity of $Cs_2NaGd_{0.35}Tb_{0.6}Eu_{0.05}Cl_6$ at various temperatures.

624 nm, corresponds to the $^5D_0 \rightarrow {}^7F_J$ transition. In Fig. 5c, $Cs_2NaGd_{0.35}Tb_{0.6}Eu_{0.05}Cl_6$ exhibits radiation stability, maintaining a constant luminescence intensity under 50 keV X-ray irradiation over 50 on–off cycles without attenuation, indicating its potential for long-term application. Notably, this compound also exhibits extraordinary thermally enhanced luminescence: the integrated emission intensity at 433 K is 1.2 times that at room temperature, and remains 1.1 times higher even at 473 K (Fig. 5d). Detailed temperature-dependent XEOL spectra of $Cs_2NaGd_{0.35}Tb_{0.6}Eu_{0.05}Cl_6$ are provided in Fig. S11 (SI), along with the intensity ratio between Eu^{3+} and Tb^{3+} (IR = I_{Eu}/I_{Tb}). As temperature increases, the IR value gradually rises from 1.4 to 2.2. Based on the temperature-dependent IR, $Cs_2NaGd_{0.35}Tb_{0.6}Eu_{0.05}Cl_6$ was proposed as a self-calibrating luminescent thermometer and its performance was further evaluated through ratiometric intensity measurements under XEOL. The relationship between IR and temperature is shown in Fig. S10b (SI) and can be fitted with the equation IR = $0.00376T + 0.43882$, with a correlation coefficient R^2 of 0.993. The absolute sensitivity (S_a) and relative sensitivity (S_r) were calculated as $S_a = 0.0038\ K^{-1}$, and S_r reaches a maximum value of 0.0034% K^{-1} at 293 K.

The physical mechanism underlying X-ray induced luminescence in $Cs_2NaGd_{1-x}Tb_xCl_6$ is schematically illustrated in Fig. 6. Upon X-ray irradiation, high-energy photons interact primarily with heavy atoms (Cs and lanthanide elements) through photoelectric and Compton effects, generating a large number of high-energy electrons and holes. These charge carriers subsequently undergo thermalization, producing a substantial quantity of secondary electrons and holes. Through transport and relaxation processes, they migrate into the conduction and valence bands, where they are eventually captured by luminescent centers. The high energy level $^6P_{7/2}$ of Gd^{3+} is situated near the conduction band, allowing carriers to be

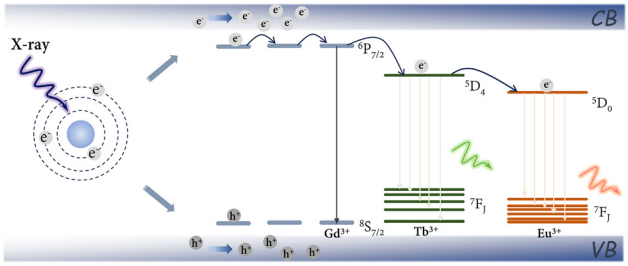

Fig. 6 Schematic illustration of the XEOL mechanism of $Cs_2NaGd_{0.35}Tb_{0.6}Eu_{0.05}Cl_6$.

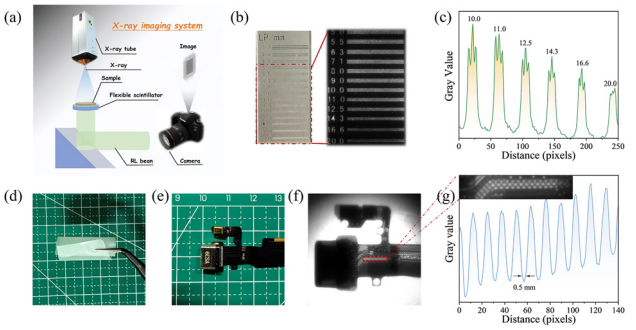

Fig. 7 (a) Schematic illustration of a home-made X-ray imaging system. The X-ray imaging of the standard line-pair card (b) and the corresponding gray value (c). (d) A curly scintillator screen based on DPLCs and PMMA. Images of a circuit board recorded under ambient light (e) and X-ray (f). (g) The gray value collected from the X-ray image of the circuit board.

readily transferred to Gd^{3+} ions. This intermediate level reduces energy loss during transfer and enhances energy transfer efficiency. In this process, Tb^{3+} ions can directly receive electrons from the CB or through non-radiative relaxation from Gd^{3+}, resulting in the characteristic emission of Tb^{3+} activators. Furthermore, in the case of Eu^{3+} co-doping, the variation in luminescence can be attributed to energy transfer from the donor Tb^{3+} to the acceptor Eu^{3+}. As temperature increases, the energy transfer efficiency from Tb^{3+} to Eu^{3+} is enhanced. This indicates that elevated temperature effectively promotes energy transfer between Tb^{3+} and Eu^{3+}, which is primarily ascribed to a thermally driven phonon-assisted energy transfer.

Utilizing the high-performance DPLC materials, an X-ray imaging system was further developed. Scintillator films were fabricated by embedding $Cs_2NaGd_{0.35}Tb_{0.6}Eu_{0.05}Cl_6$ particles into a PMMA matrix. These flexible films were prepared using a blade-coating method. First, the pre-synthesized DPLC particles were uniformly dispersed in a toluene solution containing dissolved PMMA. The mixture was then poured onto a cleaned glass substrate and spread using a blade coater with a controlled slit width. After heating at 60 °C for 30 minutes, the solidified film was peeled off from the substrate, yielding the final scintillator film. To investigate the X-ray detection limit of the proposed scintillator screen, we have included a plot of the signal-to-noise ratio (SNR) as a function of the X-ray dose rate in Fig. S12 (SI). As shown, the SNR exhibits a linear dependence on the dose rate, and the data were well fit by a linear regression. Following the conventional definition, the X-ray detection limit is determined at SNR = 3, which corresponds to a dose rate of 73.1 nGy s^{-1} films. A schematic diagram of the custom-built X-ray imaging system is shown in Fig. 7a. The scintillator films show high resolution, as quantitatively confirmed using a standard line-pair test card in Fig. 7b. As shown in Fig. 7c, a resolution of 16.6 lp mm^{-1} can be clearly distinguished, which is further validated by analyzing the corresponding gray-value profiles. As a proof, modulation transfer function (MTF) measurement using an X-ray image of the edge of a copper film was performed, as shown in Fig. S13 (SI). The calculated MTF value of 0.2 corresponds to a spatial frequency of 16.8 lp mm^{-1}, which is consistent with the resolution observed in standard line-pair phantom images. To evaluate practical applicability, X-ray imaging of representative objects was conducted. Notably, the prepared scintillator screen exhibits excellent flexibility, as shown in Fig. 7d. To evaluate its practical performance, we captured an X-ray image of an encapsulated circuit board. A comparison between the ambient light photograph (Fig. 7e) and the X-ray image (Fig. 7f) reveals clear contrast variations, which arise from differences in X-ray absorption among various materials, such as metals and plastics. In particular, the DPLCs@PMMA scintillator screen achieves high-resolution imaging as shown in Fig. 7g, enabling clear visualization of the metallic wire as small as approximately 0.5 mm, as further confirmed by the corresponding gray value analysis.

Conclusions

This work shows the successful synthesis of high-quality DPLC crystals *via* an eco-friendly supersaturation recrystallization route. The obtained $Cs_2NaTbCl_6$ exhibits a high PLQY of 73.5%. By doping with Eu^{3+}, we achieved widely tunable emission colors and excitation-dependent dynamic luminescence. Based on $Cs_2NaTb_{0.95}Eu_{0.05}Cl_6$, a typical example of an optical encryption system was demonstrated. The proposed DPCLs show exceptional performance as scintillators, featuring a high light yield, excellent thermal stability, and thermally enhanced radioluminescence. Furthermore, a ratiometric luminescence thermometer based on XEOL was developed. The practical applicability of these DPLCs was verified through the fabrication of flexible composite films, which enabled high-resolution X-ray imaging, showcasing great potential in non-destructive testing. This study provides a valuable strategy for designing high-performance lanthanide-based perovskites toward advanced optical and scintillation applications.

Author contributions

Su Zhou: writing – original draft, conceptualization, methodology and data curation. Linshuai Li: formal analysis and data curation. Gaoqing Chen: data curation. Jingtao Zhao: supervi-

sion and methodology. Lei Lei: conceptualization and writing – review & editing.

Conflicts of interest

There are no conflicts to declare.

Data availability

The data that support the findings of this study are available from the corresponding author upon reasonable request.

Supplementary information (SI) is available. Experimental section, EDS mapping, XPS spectra, XRD, decay curves, PL, PLE and XEOL spectra are provided in SI. See DOI: **https://doi.org/10.1039/d5qi02185e**.

Acknowledgements

This work was supported by the National Natural Science Foundation of China (52172164, 62475248, and 12404468) and the Zhejiang Provincial Natural Science Foundation of China under Grant No. LQN25E020001.

References

1 A. Anand, M. L. Zaffalon, A. Erroi, F. Cova, F. Carulli and S. Brovelli, Advances in Perovskite Nanocrystals and Nanocomposites for Scintillation Applications, *ACS Energy Lett.*, 2024, **9**, 1261–1287.

2 Y. Liu, A. Nag, L. Manna and Z. Xia, Lead-Free Double Perovskite $Cs_2AgInCl_6$, *Angew. Chem., Int. Ed.*, 2021, **60**, 11592–11603.

3 F. Locardi, M. Cirignano, D. Baranov, Z. Dang, M. Prato, F. Drago, M. Ferretti, V. Pinchetti, M. Fanciulli, S. Brovelli, L. De Trizio and L. Manna, Colloidal Synthesis of Double Perovskite $Cs_2AgInCl_6$ and Mn-Doped $Cs_2AgInCl_6$ Nanocrystals, *J. Am. Chem. Soc.*, 2018, **140**, 12989–12995.

4 J. H. Heo, D. H. Shin, J. K. Park, D. H. Kim, S. J. Lee and S. H. Im, High-Performance Next-Generation Perovskite Nanocrystal Scintillator for Nondestructive X-Ray Imaging, *Adv. Mater.*, 2018, **30**, 1801743.

5 W. Pan, H. Wu, J. Luo, Z. Deng, C. Ge, C. Chen, X. Jiang, W.-J. Yin, G. Niu, L. Zhu, L. Yin, Y. Zhou, Q. Xie, X. Ke, M. Sui and J. Tang, $Cs_2AgBiBr_6$ single-crystal X-ray detectors with a low detection limit, *Nat. Photonics*, 2017, **11**, 726–732.

6 Z. Wang, S. Zheng, Q. Teng, C. Li, B. Zhuang, R. Zhang, F. Huang, D. Chen and F. Yuan, Opportunity of lead-free metal halide perovskites for electroluminescence, *Innovation Mater.*, 2023, **1**, 100015.

7 Y. Zhou, J. Chen, O. M. Bakr and O. F. Mohammed, Metal Halide Perovskites for X-ray Imaging Scintillators and Detectors, *ACS Energy Lett.*, 2021, **6**, 739–768.

8 W. Zhu, W. Ma, Y. Su, Z. Chen, X. Chen, Y. Ma, L. Bai, W. Xiao, T. Liu, H. Zhu, X. Liu, H. Liu, X. Liu and Y. M. Yang, Low-dose real-time X-ray imaging with nontoxic double perovskite scintillators, *Light: Sci. Appl.*, 2020, **9**, 112.

9 Z. Gong, W. Zheng, P. Huang, X. Cheng, W. Zhang, M. Zhang, S. Han and X. Chen, Highly efficient Sb^{3+} emitters in 0D cesium indium chloride nanocrystals with switchable photoluminescence through water-triggered structural transformation, *Nano Today*, 2022, **44**, 101460.

10 Z. Tan, J. Li, C. Zhang, Z. Li, Q. Hu, Z. Xiao, T. Kamiya, H. Hosono, G. Niu, E. Lifshitz, Y. Cheng and J. Tang, Highly Efficient Blue–Emitting Bi–Doped Cs_2SnCl_6 Perovskite Variant: Photoluminescence Induced by Impurity Doping, *Adv. Funct. Mater.*, 2018, **28**, 1801131.

11 B. Yang, X. Mao, F. Hong, W. Meng, Y. Tang, X. Xia, S. Yang, W. Deng and K. Han, Lead-Free Direct Band Gap Double-Perovskite Nanocrystals with Bright Dual-Color Emission, *J. Am. Chem. Soc.*, 2018, **140**, 17001–17006.

12 H. Yang, X. Chen, Y. Chu, C. Sun, H. Lu, M. Yuan, Y. Zhang, G. Long, L. Zhang and X. Li, A universal hydrochloric acid-assistant powder-to-powder strategy for quick and mass preparation of lead-free perovskite microcrystals, *Light: Sci. Appl.*, 2023, **12**, 75.

13 X. Cheng, Z. Xie, W. Zheng, R. Li, Z. Deng, D. Tu, X. Shang, J. Xu, Z. Gong, X. Li and X. Chen, Boosting the Self-Trapped Exciton Emission in Alloyed $Cs_2Ag/NaInCl_6$ Double Perovskite via Cu^+ Doping, *Adv. Sci.*, 2022, **9**, e2103724.

14 N. Chen, T. Cai, W. Li, K. Hills-Kimball, H. Yang, M. Que, Y. Nagaoka, Z. Liu, D. Yang, A. Dong, C. Y. Xu, R. Zia and O. Chen, Yb- and Mn-Doped Lead-Free Double Perovskite Cs_2AgBiX_6 (X = Cl^-, Br^-) Nanocrystals, *ACS Appl. Mater. Interfaces*, 2019, **11**, 16855–16863.

15 S. Jin, R. Li, H. Huang, N. Jiang, J. Lin, S. Wang, Y. Zheng, X. Chen and D. Chen, Compact ultrabroadband light-emitting diodes based on lanthanide-doped lead-free double perovskites, *Light: Sci. Appl.*, 2022, **11**, 52.

16 S. Jin, H. Yuan, T. Pang, M. Zhang, Y. He, B. Zhuang, T. Wu, Y. Zheng and D. Chen, Boosting STE and Nd^{3+} NIR Luminescence in $Cs_2AgInCl_6$ Double Perovskite via Na^+/Bi^{3+}–Induced Local Structure Engineering, *Adv. Funct. Mater.*, 2023, **33**, 2304577.

17 F. Schmitz, K. Guo, J. Horn, R. Sorrentino, G. Conforto, F. Lamberti, R. Brescia, F. Drago, M. Prato, Z. He, U. Giovanella, F. Cacialli, D. Schlettwein, D. Meggiolaro and T. Gatti, Lanthanide-Induced Photoluminescence in Lead-Free $Cs_2AgBiBr_6$ Bulk Perovskite: Insights from Optical and Theoretical Investigations, *J. Phys. Chem. Lett.*, 2020, **11**, 8893–8900.

18 S. Wang, J. Qi, S. V. Kershaw and A. L. Rogach, Co-Doping of Cerium and Bismuth into Lead-Free Double Perovskite $Cs_2AgInCl_6$ Nanocrystals Results in Improved Photoluminescence Efficiency, *ACS Nanosci. Au*, 2022, **2**, 93–101.

19 Z. Rao, X. Zhao and X. Gong, Rare–Earth–Based Lead–Free Halide Double Perovskites for Light Emission: Recent Advances and Applications, *Adv. Funct. Mater.*, 2024, **34**, 2406424.

20 P. Saghy, A. M. Brown, C. Chu, L. C. Dube, W. Zheng, J. R. Robinson and O. Chen, Lanthanide Double Perovskite Nanocrystals with Emissions Covering the UV–C to NIR Spectral Range, *Adv. Opt. Mater.*, 2023, **11**, 2300277.
21 G. Gundiah, K. Brennan, Z. Yan, E. C. Samulon, G. Wu, G. A. Bizarri, S. E. Derenzo and E. D. Bourret-Courchesne, Structure and scintillation properties of Ce^{3+}-activated $Cs_2NaLaCl_6$, Cs_3LaCl_6, $Cs_2NaLaBr_6$, Cs_3LaBr_6, Cs_2NaLaI_6 and Cs_3LaI_6, *J. Lumin.*, 2014, **149**, 374–384.
22 J. H. Han, T. Samanta, Y. M. Park, H. J. Kim, N. S. M Viswanath, H. W. Kim, B. K. Cha, S. B. Cho and W. B. Im, Highly Stable Zero-Dimensional Lead-Free Metal Halides for X-ray Imaging, *ACS Energy Lett.*, 2022, **8**, 545–552.
23 E. C. Samulon, G. Gundiah, M. Gascón, I. V. Khodyuk, S. E. Derenzo, G. A. Bizarri and E. D. Bourret-Courchesne, Luminescence and scintillation properties of Ce^{3+}-activated $Cs_2NaGdCl_6$, Cs_3GdCl_6, $Cs_2NaGdBr_6$ and Cs_3GdBr_6, *J. Lumin.*, 2014, **153**, 64–72.
24 C. Zhao, Y. Gao, J. Wang and J. Qiu, Achieving Nearly Quantitative (~100%) IQE and 42.3% EQE Across NIR–I and NIR–II Regions with Cr^{3+}-doped $Cs_2NaScCl_6$ under 300 nm Excitation, *Laser Photonics Rev.*, 2023, **18**, 2300952.
25 W. Zhou, Y. Yu, P. Han, C. Li, T. Wu, Z. Ding, R. Liu, R. Zhang, C. Luo, H. Li, K. Zhao, K. Han and R. Lu, Sb-Doped Cs_3TbCl_6 Nanocrystals for Highly Efficient Narrow-Band Green Emission and X-Ray Imaging, *Adv. Mater.*, 2024, **36**, e2302140.
26 Q. Guo, L. Wang, L. Yang, J. Duan, H. Du, G. Ji, N. Liu, X. Zhao, C. Chen, L. Xu, L. Gao, J. Luo and J. Tang, Spectra stable deep-blue light-emitting diodes based on cryolite-like cerium(III) halides with nanosecond d-f emission, *Sci. Adv.*, 2022, **8**, eabq2148.
27 H. W. Kim, J. H. Han, H. Ko, T. Samanta, D. G. Lee, D. W. Jeon, W. Kim, Y.-C. Chung, W. B. Im and S. B. Cho, High-Throughput Screening on Halide Perovskite Derivatives and Rational Design of Cs_3LuCl_6, *ACS Energy Lett.*, 2023, **8**, 3621–3630.
28 M. Lee, D. H. D. Lee, S. V. Hong, H. Y. Woo, J. Y. Chae, D. W. Lee, M. J. Han and T. Paik, Highly Luminescent and Multifunctional Zero–Dimensional Cesium Lanthanide Chloride Cs_3LnCl_6 Colloidal Nanocrystals, *Adv. Opt. Mater.*, 2022, **10**, 2102727.
29 Y. Shi, X. Zhang, X. Wang and Y. Zhang, Pure Green Upconversion from a Multicolor Downshifting Perovskite Crystal, *Adv. Opt. Mater.*, 2023, **11**, 2202704.
30 L. Sun, B. Dong, J. Sun, Y. Wang, R. Sun, S. Hu, B. Zhou, W. Xu, X. Bai, L. Xu, D. Zhou and H. Song, Fabrication, Optical Property, and White LED Application of Novel Lanthanide–Based Family Cs_2NaLnX_6 (X = Cl, Br, I) Perovskite Nanomaterials, *Laser Photonics Rev.*, 2023, **17**, 2300045.
31 L. Sun, B. Dong, J. Sun, Y. Wang, Y. Wang, S. Hu, B. Zhou, X. Bai, L. Xu, D. Zhou and H. Song, Efficient and Stable Multicolor Emissions of the Coumarin-Modified Cs_3LnCl_6 Lead-Free Perovskite Nanocrystals and LED Application, *Adv. Mater.*, 2024, **36**, e2310065.
32 M. Wang, X. Chen, F. Zhang, Z. Ma, X. Ji, S. Cheng, G. Pan, D. Wu, X. J. Li, Y. Zhang, C. Shan and Z. Shi, Colloidal Synthesis of Blue-Emitting Cs_3TmCl_6 Nanocrystals via Localized Excitonic Recombination for Down-Conversion White Light-Emitting Diodes, *ACS Nano*, 2024, **18**, 30421–30432.
33 K. Nie, X. Zhang, X. Zhang, X. Zhang, L. Wang, J. Xu, L. Mei and H. Wang, Lead-free double perovskites with near-unity photoluminescence quantum yield for flexible anti-counterfeiting fibers and optoelectronic devices, *Chem. Eng. J.*, 2025, **508**, 161093.
34 H. Peng, X. Wang, W. Huang, S. Yu, L. Kong, Q. Wei, J. Zhao and B. Zou, Efficient tunable visible and near-infrared emission in Sb^{3+}/Sm^{3+}-codoped $Cs_2NaLuCl_6$ for near-infrared light-emitting diode, triple-mode fluorescence anti-counterfeiting and information encryption, *Chin. Chem. Lett.*, 2024, **35**, 109462.
35 R. Sun, M. Jia, X. Chen, F. Zhang, Z. Ma, Y. Liu, J. Zhang, L. Lian, Y. Han, M. Li, D. Yang, X. Li, Y. Zhang, C. Shan and Z. Shi, Constructing Efficient and Thermostable Red–NIR Emitter via Cross Relaxation and Crystal–Field Engineering of Holmium–Based Perovskite–Type Half Metal, *Laser Photonics Rev.*, 2023, **18**, 2301028.
36 Q. Duan, Y. Xu, Y. Zha, F. Meng, Q. Wang, Y. Wen and J. Qiu, Near-Complete Suppression of NIR-II Luminescence Quenching in Halide Double Perovskites for Surface Functionalization Through Facet Engineering, *Adv. Sci.*, 2024, **11**, 2403198.
37 Q. Hu, Z. Deng, M. Hu, A. Zhao, Y. Zhang, Z. Tan, G. Niu, H. Wu and J. Tang, X-ray scintillation in lead-free double perovskite crystals, *Sci. China: Chem.*, 2018, **61**, 1581–1586.
38 X. Wang, X. Zhang, S. Yan, H. Liu and Y. Zhang, Nearly-Unity Quantum Yield and 12-Hour Afterglow from a Transparent Perovskite of $Cs_2NaScCl_6$:Tb, *Angew. Chem., Int. Ed.*, 2022, **61**, 202210853.
39 V. Naresh, P.-R. Cha and N. Lee, $Cs_2NaGdCl_6$:Tb^{3+}—A Highly Luminescent Rare-Earth Double Perovskite Scintillator for Low-Dose X-ray Detection and Imaging, *ACS Appl. Mater. Interfaces*, 2024, **16**, 19068–19080.
40 Z. Wang, X. Xu, S. Wang, H. Xu, W. Xu, Q. Zeng, G. Deng, Y. Jiang and S. Wu, Cerium Doping Double Perovskite Scintillator for Sensitive X-ray Detection and Imaging, *Chemistry*, 2021, **27**, 9071–9076.
41 W. Zhou, C. Li, T. Wu, R. Liu, Z. Ding, R. Zhang, Y. Yu, P. Han and R. Lu, Bright Green-Emitting All-Inorganic Terbium Halide Double Perovskite Nanocrystals for Low-Dose X-ray Imaging, *J. Phys. Chem. Lett.*, 2023, **14**, 8577–8583.
42 A. M. Afridi, N. A. Nipa and M. A. Rashid, First-principle investigation of lead-free double perovskites Cs_2MScCl_6 (M = Na, K) for optoelectronic and thermoelectric applications, *Phys. Scr.*, 2024, **99**, 055938.
43 M. Atanasov, C. Daul, H. U. Güdel, T. A. Wesolowski and M. Zbiri, Ground States, Excited States, and Metal-Ligand Bonding in Rare Earth Hexachloro Complexes: A DFT-Based Ligand Field Study, *Inorg. Chem.*, 2005, **44**, 2954–2963.